Downloaded from orbit.dtu.dk on: Jun 03, 2024

DTU Library

On the thermoelectric properties of Nb-doped $SrTiO_3$ epitaxial thin films

Chatterjee, Arindom; Lan, Zhenyun; Christensen, Dennis Valbjørn; Bauitti, Federico; Morata, Alex; Chavez-Angel, Emigdio; Sanna, Simone; Castelli, Ivano E.; Chen, Yunzhong; Tarancon, Albert

Total number of authors:
11

Published in:
Physical Chemistry Chemical Physics

Link to article, DOI:
10.1039/d1cp03679c

Publication date:
2022

Document Version
Peer reviewed version

Link back to DTU Orbit

Citation (APA):
Chatterjee, A., Lan, Z., Christensen, D. V., Bauitti, F., Morata, A., Chavez-Angel, E., Sanna, S., Castelli, I. E., Chen, Y., Tarancon, A., & Pryds, N. (2022). On the thermoelectric properties of Nb-doped $SrTiO_3$ epitaxial thin films. *Physical Chemistry Chemical Physics*, *24*(6), 3741-3748. https://doi.org/10.1039/d1cp03679c

General rights
Copyright and moral rights for the publications made accessible in the public portal are retained by the authors and/or other copyright owners and it is a condition of accessing publications that users recognise and abide by the legal requirements associated with these rights.

- Users may download and print one copy of any publication from the public portal for the purpose of private study or research.
- You may not further distribute the material or use it for any profit-making activity or commercial gain
- You may freely distribute the URL identifying the publication in the public portal

If you believe that this document breaches copyright please contact us providing details, and we will remove access to the work immediately and investigate your claim.

On the thermoelectric properties of Nb-doped $SrTiO_3$ epitaxial thin films

Arindom Chatterjee[a], Zhenyun Lan[a], Dennis Valbjørn Christensen[a], Federico Bauitti [b], Alex Morata [b], Emigdio Chavez-Angel[c], Simone Sanna[a, d], Ivano E. Castelli[a], Yunzhong Chen[a], Albert Tarancon, [b,e] and Nini Pryds [a*]

[a] Department of Energy Conversion and Storage, Technical University of Denmark, 2800 Kgs Lyngby, Denmark; [b] Catalonia Institute for Energy Research (IREC), Jardins de Les Dones de Negre 1, 08930 Sant Adria' Besos, Barcelona, Spain; [c]Catalan Institute of Nanoscience and Nanotechnology (ICN2), and Barcelona. Institute of Science and Technology (BIST), Bellaterra-08193, Spain; [d] UNIVERSITA' DEGLI STUDI DI ROMA TOR VERGATA and CNR-SPIN Rome, Department of Civil Engineering and Computer Science, Università di Roma Tor Vergata Dipartimento di Ingegneria Civile e Ingegneria Informatica DICII, Via del Politecnico - 1, I - 00133, Roma, Italy; [e] ICREA, 23 Passeig Lluís Companys, Barcelona 08010, Spain

*corresponding author- Nini Pryds (nipr@dtu.dk)

Keywords:

Nb-doped $SrTiO_3$, epitaxial thin films, pulsed laser deposition, strain, thermoelectricity, scattering mechanism

Abstract

The exploration for thermoelectric thin films of complex oxides such as $SrTiO_3$-based oxides is driven by the need for miniaturized harvesting devices for powering the Internet of Things (IoT). However, there is still not a clear consensus in the literature for the underlying influence of film thickness on thermoelectric properties. Here, we report the fabrication of epitaxial thin films of 6% Nb-doped $SrTiO_3$ on (001) $(LaAlO_3)_{0.3}(Sr_2AlTaO_6)_{0.7}$ (LSAT) single crystal using pulsed laser deposition (PLD) where the film thickness was varied from 2 nm to 68 nm. The thickness dependence shows a subtle increase of tetragonality of the

thin film lattice and a gradual drop of the electrical conductivity, the density of charge carriers, and the thermoelectric Seebeck coefficient as the film thickness decreases. DFT-based calculations show that ~2.8% increase in tetragonality results in an increased splitting between t_{2g} and e_g orbitals to 42.3 meV. However, experimentally observed tetragonality for films between 68 to 13 nm is only 0.06%. Hence, the effect of thickness on tetragonally is neglected. We have discussed the decrease of conductivity and the Seebeck coefficient based on the decrease of carriers and change in the scattering mechanism, respectively.

Introduction

$SrTiO_3$ (STO)-based thin films offer a large variety of physical properties such as metal-insulator transition[1], ferro-[2], piezo-[3], pyro-[4] and flexo-electricity[5], high thermopower[6], ferromagnetism[7,8], superconductivity[9], high electron mobility at low temperatures[10–12] and resistive switching[13], making STO the "working horse" of many oxide-based devices. Since the physical properties of the films depend on the chemical composition and the fabrication conditions, careful control of deposition parameters is generally necessary for achieving the desired properties.

Realization of unusual high thermopower (or Seebeck coefficient) due to the formation of high-density 2-dimensional electron gas (2DEGs)[6] and its tunability by electric field[14,15,16] in $SrTiO_3$ make it potentially important for fundamental studies as well as for thin film-based thermoelectric applications. Nb-doping in Ti-site of $SrTiO_3$ makes it an *n*-type conductor, which exhibits good thermoelectric properties[17–20,21]. Generally, the appropriate doping level for optimized thermoelectric performance depends on the balance between the electrical conductivity (σ) and the Seebeck coefficient (S), leading to a high thermoelectric power factor ($S^2\sigma$)[22]. In the literature, it is shown that the Nb-doping in pristine insulating $SrTiO_3$ (Nb:STO) thin films can induce a metallic phase in these films, and the highest σS^2 of ≈2.6 $mWm^{-1}K^{-2}$ for Nb:STO thin films was achieved near room temperature for the films which are doped between 5-8% Nb[17,21].

The growth of pristine and doped STO thin films with desired chemical compositions and high crystal quality is often obtained using pulsed laser deposition (PLD)[23–29,30]. The fabricated films are dependent on the process parameters such as the pO_2 atmosphere in the chamber, deposition temperature, laser fluence, and lattice match between the substrate and film[20,31]. If the growth conditions

are carefully chosen, high-quality films can be achieved by PLD, such as Nb-doped STO films with high electron mobility exceeding μ ~ 53700 $cm^2V^{-1}s^{-1}$ at 2K[11]. Other deposition techniques such as molecular beam epitaxy (MBE) allow nearly stoichiometric La-doped STO films with high electron mobility of (μ ~ 50000 $cm^2V^{-1}s^{-1}$ at 2K) and a high Seebeck coefficient (S~ -650 μVK^{-1} at 20 K)[32]. Nevertheless, regardless of the physical deposition technique, the electronic properties of doped STO thin film suppress as the film thickness reduces[29,33–35] and below a critical thickness of 4-5 unit cells[34,35] film become electronically dead[29,34]. This behavior is often associated with a decrease in the carrier density[29,34,35].

A few possibilities have been proposed in the literature to address the loss of itinerant carriers below the critical thickness such as i) decomposition into electrically insulating secondary phases or formation of other oxide insulating phases[36]; ii) formation of large oxygen vacancy clusters, which can trap the free charge carriers[37,38]; iii) local stoichiometric changes, structural deformation, and defects[20,31] and iv) formation of electron depletion layer (EDL) at the surface of film[29]. However, to date, it remains elusive why the carrier density shows such a strong thickness dependence. Studying the Seebeck effect might provide insight into this question as it is directly linked with the electronic band structure.

In this paper, we report how the transport properties and the Seebeck coefficient depend on the film thickness for 6% Nb-doped STO films deposited on single crystalline (001) $(LaAlO_3)_{0.3}(Sr_2AlTaO_6)_{0.7}$ (LSAT). The thickness was varied in the range from 2 nm to 68 nm. Our results show that the conductivity and carrier density decrease as the film thickness reduces. However, in contrast to the conventional trend where a low carrier density results in a high Seebeck coefficient, the thinnest film result in both a systematic lowering of the Seebeck coefficient and charge carrier density. Our analysis suggests that the scattering mechanism might play a significant role to explain our observations.

1. Experiments and atomistic simulations

Epitaxial Nb:STO thin films were grown by PLD on 5×5×0.5 mm^3 (001)-LSAT single crystal substrates with a lattice constant of a = 3.870 Å supplied from CrysTec GmbH. The as-received substrates were cleaned with acetone and ethanol before thin film deposition. A careful experimental study using PLD showed that stoichiometric STO films can be achieved only at a very narrow range of laser fluence and oxygen partial pressure (pO_2)[25]. Following this study, we use a fluence of ~1.1 Jcm^{-2} at a repetition rate of 10 Hz (KrF

excimer, λ= 248 nm) and varied the pO_2 from 10^{-3} to 2×10^{-5} mbar. The distance between the target and the substrate was kept constant at 70 mm. All the depositions were carried out at 700 °C and no post-annealing treatments were performed.

Structural analysis of the as-grown films was carried out by standard X-ray diffraction in a 2θ/ω configuration using Panalytical X´pert pro-MRD diffractometer. The thicknesses of the films were determined using X-ray reflectivity (XRR) and ellipsometry techniques with a mutual agreement as shown in Fig. S1, Supporting information, SI. The in-plane and the out-of-plane lattice constants of the films were calculated from the standard 2θ/ω and x-ray reciprocal space maps (RSMs), respectively. The morphology of the film surface was characterized by an atomic force microscope (AFM).

Electrical conductivity measurements were carried out in a van der Pauw configuration. The Seebeck coefficient was measured from 20 to 290 K as schematically illustrated in Fig. S2a-b, SI. The measurements were carried out using a Cr (5 nm)/Pt (50 nm) heater and two Cr (5 nm)/Pt (50 nm) resistors/thermometers which were patterned on the top of the thin-film surface using optical lithography. The Cr/Pt line heater was electrically isolated from the rest of the film in order to avoid any current leakage from the heater to the film. Prior to the Seebeck measurements, the resistance of the resistors/thermometers was calibrated as a function of the cryostat temperature, and a look-up table relating the resistance to the temperature was prepared (see Fig. S2c, SI). At a fixed cryostat temperature, a variable amount of constant current was applied to the on-chip Cr/Pt heater in order to generate in-plane thermal gradients. Temperature gradients (ΔT) were measured by using the previously calibrated resistance of the thermometers. Approximately ΔT~1K was achieved at 255K cryostat temperature on applying 17 mA current to the on-chip heater. The Seebeck voltage and the temperature gradients were measured simultaneously (see Fig. S2d-e, SI). The magnitude and the sign of Seebeck coefficients were evaluated from the slope of -ΔV vs ΔT curve as shown in Fig. S2f. LSAT substrates were chosen for this study due to their lower thermal conductivity, compared to the other substrates such as MgO.[39] Lower thermal conductivity of substrate will allow stabilizing a larger temperature gradient for Seebeck coefficient measurements in a given heater-power.

Density functional theory (DFT) calculations were performed using the strongly constrained and appropriately normed (SCAN) meta-GGA exchange-correlation[40] functional as implemented in the Vienna

ab-initio simulation package (VASP)[41,41]. The Brillouin zone was sampled with a 6 x 6 x 6 Γ-centered k-point grid for the Nb-doped supercell (40 atoms). The experimental measured thin film lattice parameters (one is *a*=*b*=3.870 Å, *c*=3.906 and the other is *a*=*b*=3.870 Å, *c*=3.980 Å) were used. A plane wave cut of 875 eV was used. The structures were relaxed until the force on each atom was less than 0.01 eV/Å.

2. Results and discussion

Nb-doping in the $SrTiO_3$ film is evident from the change in lattice parameters, and electronic conductivity measurements (not shown). A set of Nb:STO films with different thicknesses ranging from 2 to 68 nm was deposited. Standard x-ray diffraction patterns of 68 nm thick Nb:STO film (Fig. S3, SI) show reflections which only belong to the film without any sign of impurity phases. The reflections from the film can be indexed with (00*l*) indices, which point toward the *c*-axis (normal to the film). The *c*-parameter is ~3.970 Å. Films with lower thicknesses show Keissig fringes on the side of 002 films reflections, which indicates high-quality interfaces between the film and the LSAT substrate and homogeneous film thickness throughout the films. AFM topography images show that the surfaces of all the films are extremely flat, and no change in surface morphology is observed as a function of film thickness (see Fig. S5).

The temperature and thickness dependence of the conductivity and Seebeck coefficient are summarized in Fig. 1. Due to the heavy Nb doping (6%), the Nb:STO films show metallic-like electronic conductivity. The heating-cooling cycles of the conductivity measurements were reversible within the range of the temperature 300 to 473K in air. The measurement of the conductivity was kept at a temperature below 475 K in order to avoid any degradation of the films[42]. As shown in Fig. 1a, the conductivity of the 68 nm film decreases from 605 to 545 S/cm as the temperature increases from 300 to 475 K. Films with lower thicknesses between 45 and 13 nm show a similar behavior except that the magnitude of conductivity at around 300 K dropped significantly. Upon further decrease of the film thickness to 5 nm film, the conductivity dropped drastically to ≈1 S/cm and the conductivity is lowered when the temperature is lowered, indicating an insulating-like behavior. Interestingly, the films below a critical thickness of 2 nm are electrically insulating, and show the known behavior of "dead layers". Notably, a 2DEG is not formed at the interface between the LSAT substrate, and the Nb-doped STO film. In an earlier study[43], STO films were deposited on the LSAT substrates to examine the interface conductivity, but no indication of a 2DEG was found.

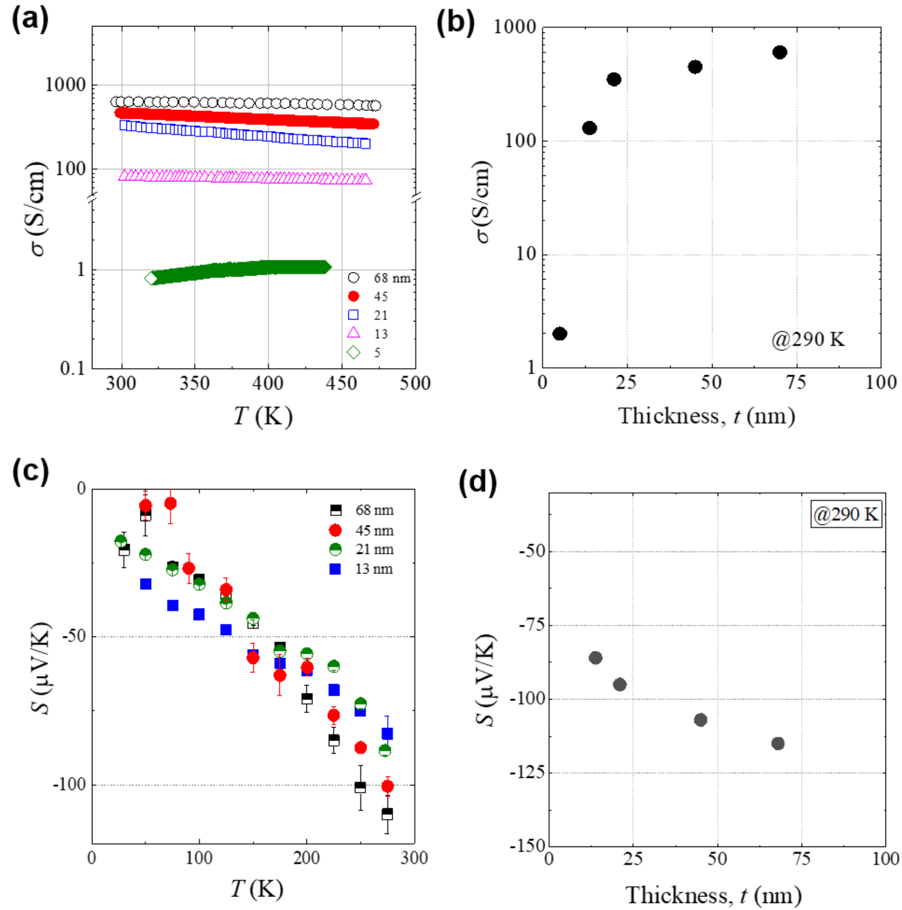

Fig. 1 Temperature and thickness dependence on the thermoelectric transport properties of Nb:STO films grown on LSAT substrates. a) Temperature dependence on the electrical conductivity for Nb:STO film of variable thicknesses. b) Room temperature electrical conductivity as a function of the film thickness. c) Temperature dependence on the Seebeck coefficients of Nb:STO film of variable thicknesses. d) Seebeck coefficient at room temperature as a function of the film thickness.

Linear temperature dependence of the Seebeck coefficient is expected for metals or degenerate band semiconductors[44]. The negative sign of the Seebeck coefficient measured in all the films confirms the *n*-type conductivity in Nb:STO films. As shown in Fig. 1c, the temperature dependence of Seebeck coefficient (S(T)) of the 68 nm thick film shows a continuous decrease from -21 to -118 μV/K when the temperature increases from 20 to 290 K. Similarly, the magnitude of the Seebeck coefficient for a 45 nm film drops slightly down to -100 μV/K at 290 K but the $S(T)$ remains approximately linear. The measurement of the Seebeck coefficient at relatively higher temperatures, between 300 to 550 K, for the 45 nm thick film shows a continuous decrease to –215 μV/K at 540 K, which shows a good agreement with the linear

extrapolation of $S(T)$ as shown in Fig. S4. When further decreasing the film thickness down to 13 nm, the magnitude of the Seebeck coefficient drops to -86 μV/K at 290 K. Interestingly, the slope of the S(T) curve seems to decrease as the thickness of the films decreases. No reliable Seebeck coefficients could be measured for ultrathin 5 nm film as the resistance of the film at this thickness was very high.

Fig. 1b and d depict thickness dependence of conductivity and Seebeck coefficient at 290 K, respectively. Two interesting observations are worth pointing out here: i) there is a critical thickness, approximately at 5 nm, below which electronic and thermoelectric properties of Nb:STO films diminish and; ii) relatively lower value of the Seebeck coefficients are obtained at lower conductivities, which is unusual behavior.

To investigate this, the temperature dependencies of charge carrier density and mobility were measured for films with two different thicknesses, i.e., 32 and 11 nm. This was extracted from the Hall resistances, which were linear in the entire magnetic field range from -5T to 5T and temperature range from 20 to 300 K. The carrier density for the 32 nm film ($n_{32\ \mathrm{nm}}$) shows a weak temperature dependence with a drop from 1.7×10^{21} to 1.4×10^{21} cm^{-3} when the temperature decreases from 300 to 25 K respectively, while for the 11 nm film ($n_{11\mathrm{nm}}$), it drops from 9.5×10^{20} cm^{-3} at 300 K to 5.5×10^{20} cm^{-3} at 25 K, as depicted in Fig. 2a-b. Such a temperature dependence of the carrier was observed previously for La-doped STO films and interpreted as an increase in the thickness of the dead-layer at lower temperatures[29] where STO attains a large dielectric constant[29,45]. Mobility of film continuously increases on decreasing temperature 300 to 20K, and below20K, it shows a saturating behavior. This trend is typically observed in bulk $SrTiO_3$ or $SrTiO_3$-based heterostructures[46]. Nevertheless, both carrier density and electron mobility drop significantly at all temperatures in our case as the film thickness decreases, which results in a dramatic drop in conductivity as film thickness reduces.

The decrease in mobility can be explained due by the decrease of the effective mass of electrons (m^*) or an increase in scattering time (τ). Our density functional theory (DFT)-based calculations suggest that there is no significant change in the effective mass of electrons when the thickness is reduced. In the case of thickness dependence calculations of effective masses, 4.5 and 8.5 supercells were taken into consideration, as depicted in Fig. S6, and Fig. S7. The effective mass is obtained by fitting a quadratic function ($y=A+Bx+Cx^2$) at the band edge from the first conduction band as shown in Fig. S8. It is likely

therefore that the scattering time, which is related to the scattering mechanisms, dominates the mobility for films with different thicknesses.

The formation of defects or vacancy clusters can trap free charge carriers, as mentioned earlier. Such an indication arises from the measured out-of-plane lattice constants. As shown in Fig. 2d, the in-plane lattice constants of 68 and 21 nm thin films are fully coherent with the LSAT substrates i.e. films are fully strained in-plane. Assuming a lattice constant of a = 3.922 Å for the bulk polycrystalline $SrTi_{0.94}Nb_{0.06}O_3$, [47] one can calculate an in-plane lattice mismatch of about ~ -1.33%, (see SI for details). Therefore, the films are expected to display an out-of-plane distortion in response to the in-plane compressive strain. However, the calculated c = 3.934 Å using a Poisson ratio of v=0.23[48] for strained 68 nm film is lower than the experimentally measured one, 3.970 Å. The discrepancy between the measured and calculated lattice parameters points towards an in-elastic lattice distortion along the out-of-plane direction. This could be explained due to the deviation of film stoichiometry from its nominal composition[45]. The determination of the types and concentration of defects in our films is beyond the scope of this paper. The variation of the measured c-parameters as a function of film thickness shows (see Fig. 2c) a subtle increase (Δc=0.0025 Å) for the film thickness between 68 and 13 nm. Such a small variation in the out-of-plane parameter is within the error range of calculating lattice parameters from XRD. Hence, the effect of thickness on tetragonality is neglected.

Usually, a decreasing carrier density results in an increase in the Seebeck coefficient in semiconductors[49]. Seebeck coefficient is expected to be proportional to the effective mass of carriers and expected to increase with the $n^{2/3}$ according to the single parabolic band model[50]. Our data, however, do not show the expected trend. As shown earlier in Fig. S6, and S7, the effective mass of electron bands calculated from our DFT-based electronic structure does not show any significant variation as a function of film thickness. These experimental findings lead us to consider the presence of some competing factors other than the mass of the electrons (m^*), such as the scattering mechanism (r, which is related to energy-dependent scattering time: $\tau(E) = \tau_0 E^r$), and/or electron band degeneracy (z) dominate the magnitude of the Seebeck coefficient.

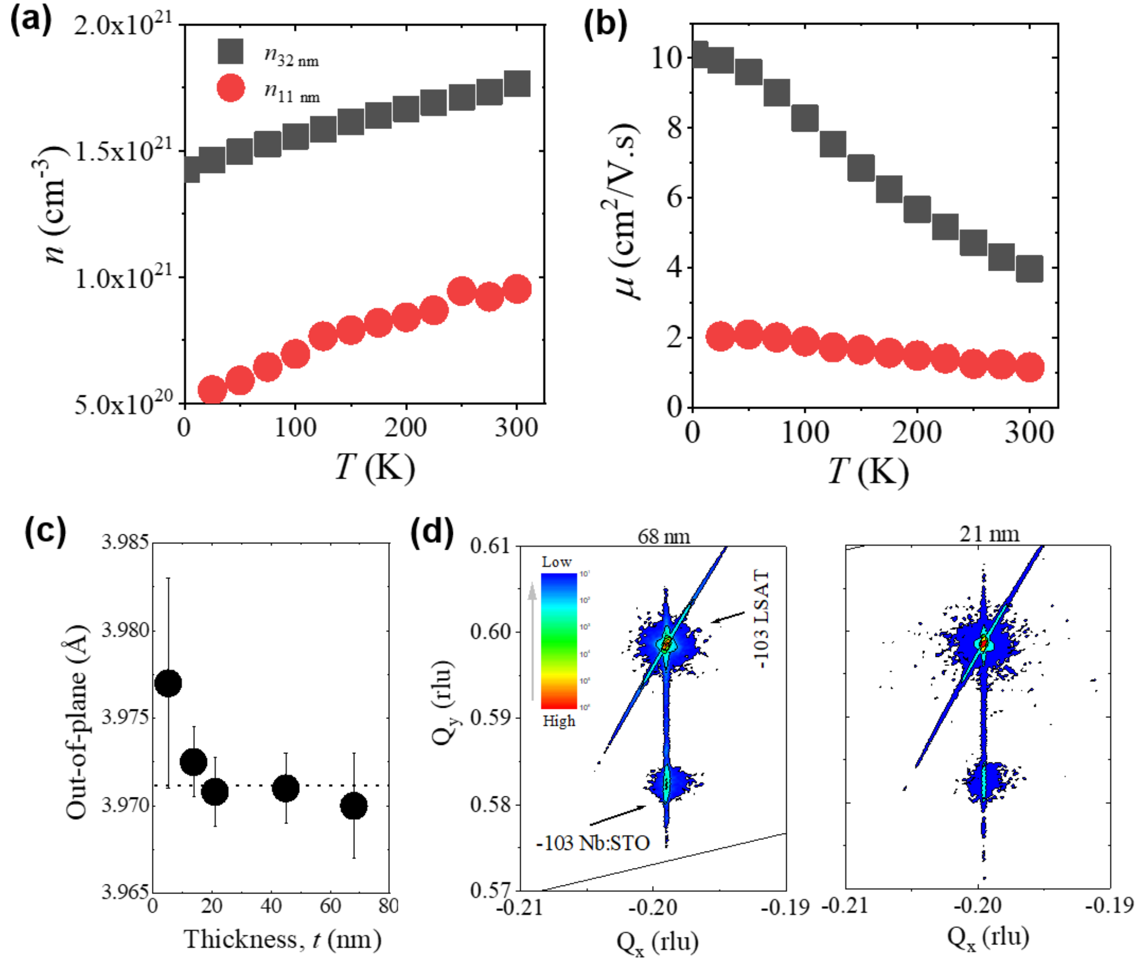

Fig. 2 a-b) temperature dependence on the density of charge carriers (n) and electron mobility (μ) of 32 and 11 nm thick Nb:STO films grown on LSAT substrates: n drops as film thickness reduces. c) Thickness dependence on the out-of-plane lattice parameters showing an increase of tetragonality for the ultrathin film. d-e) Reciprocal space maps around -103 film and substrate reflections and out-of-plane lattice parameters as a function of film thickness show that all the films are fully strained in-plane with the LSAT substrates.

The changes in tetragonality of Nb:STO films can influence the Seebeck coefficient by lifting the degeneracy[20]. To illustrate, theoretically, the possible effect of tetragonality on the electronic structure, we have carried out DFT calculations by using a fixed in-plane (a=3.870 Å) and a variable out-of-plane lattice constant (c= 3.870, 3.905, 3.970, and 3.979 Å). The band gaps obtained for different c-parameters are summarized in Table S3. As can be seen from the orbital projected densities of states in Fig. 3a, the t_{2g} orbitals (d_{xy}, d_{yz}, d_{xz}) are degenerate in the cubic case where a=c. The t_{2g} orbitals split into a low energy doublet (d_{xz}, d_{yz}) and a high energy singlet (d_{xy}) with the energy difference increasing monotonically up to

approx. 40 meV as the tetragonality increases up to ~2.8% (see Table S1, SI), which agrees well with the other theoretical calculations[50]. However, experimentally observed tetragonality for films between 68 to 13 nm film is only 0.06%, and so the effect of tetragonality on band structure is neglected. Due to the heavy Nb doping concentration (6%) in $SrTiO_3$ the Fermi level shifts in the conduction band, which also suggests that the effect of tetragonality on the band degeneracy is very small. The overall band degeneracy for our Nb:STO films can, therefore, be considered either 6 or 4.

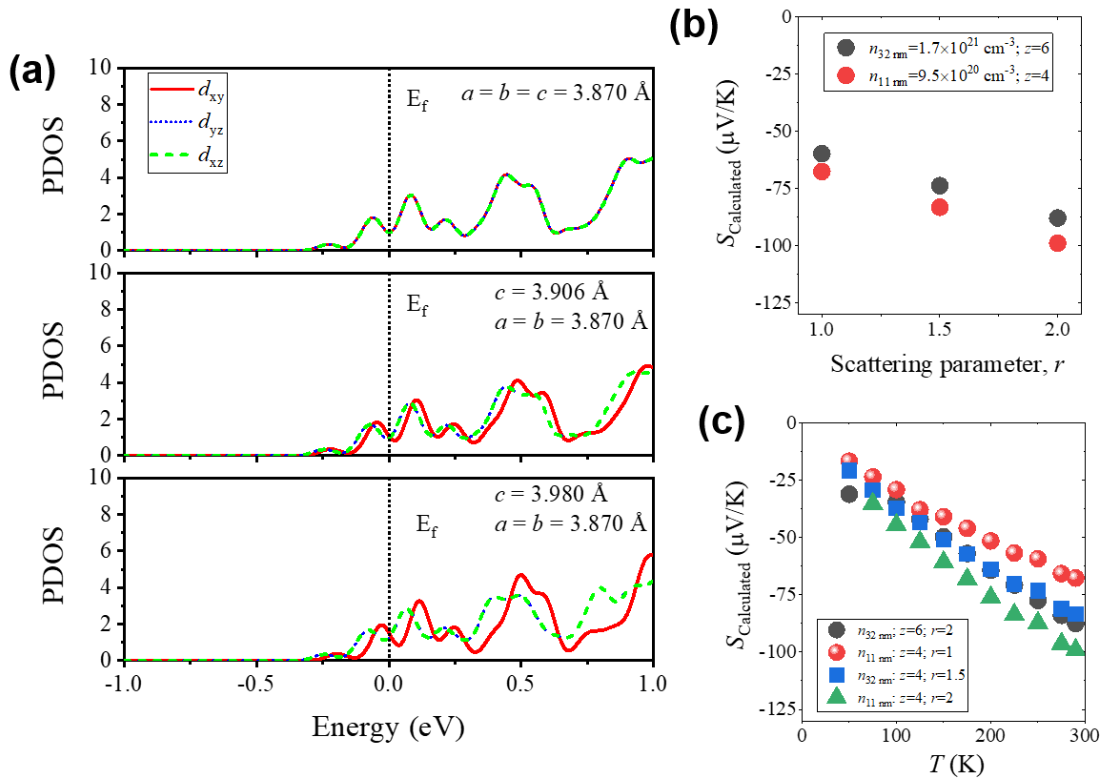

Fig. 3 Orbital projected densities of states: the t_{2g} orbitals (d_{xy}, d_{yz}, d_{xz}) split into a low energy doublet (d_{xz}, d_{yz}) and a high energy singlet (d_{xy}) for c=3.980 Å (2.84% tensile strain in c-direction), while it shows little splitting for c =3.906 Å and no splitting for c= 3.870 Å. (b)- Calculated Seebeck coefficient as a function of *r* (*r* is scattering parameter) at a fixed *z*. (c) Calculated temperature dependence on Seebeck coefficient at variable r from the measure *n*.

To illustrate the effect of the scattering parameter transparently, the relative change of Seebeck coefficients (ΔS) due to lowering the *r* (from *r*=2 to *r*=1) is calculated by using equations (1-4) from the estimated chemical potential (η), independently[20,51,52].

$$S = \frac{k_B}{e}\left[-y + \delta_r(y)\right] \qquad (1)$$

$$\delta_r(y) = \frac{(r+2)F_{r+1}(y)}{(r+1)F_r(y)} \qquad (2)$$

$$F_r(y) = \int_0^\infty \frac{x^r}{1+e^{x-y}}\,dx \qquad (3)$$

$$n = z\left(\frac{2\pi m^* k_B T}{h^2}\right)^{\frac{3}{2}} \frac{2}{\sqrt{\pi}} F_{\frac{1}{2}}(y) \qquad (4)$$

In equation (1-4), $y\ (= \eta/k_B T)$, r and F_r are the reduced chemical potential, scattering parameter, and Fermi integral, respectively. For calculating chemical potential from our measured density of carriers by using equation (4), we have taken $m^* \approx 1.1 m_0$ (where m_0 is the rest mass of the electron)[18] and z =4 or 6.[51] Experimentally measured carriers ($n_{32\text{ nm}}$=1.7×10^{21} cm^{-3} and $n_{11\text{ nm}}$=9.5×10^{20} cm^{-3}) were used to calculate the chemical potential, which, in turn, yielded Seebeck coefficient at 290 K as shown in Fig. 3b. Seebeck coefficient decreases monotonically as the scattering parameter decreases at any fixed n and z. Note that the calculated Seebeck coefficient for $n_{11\text{ nm}}$ is higher than that for $n_{32\text{ nm}}$ at all r values as $n_{32\text{ nm}} > n_{11\text{ nm}}$. It is important to note here that the density of electronic states obtained from our DFT-based calculations were not used to estimate Seebeck coefficient by using Boltzmann transport theory.

The relative drop of the calculated Seebeck, ΔS ~ -28 µV/K, is obtained for $n_{32\text{ nm}}$ when r varies from 2 to 1, where r is related to the type of scattering mechanism involved in the conduction process (Fig. 3b). To illustrate further the role of the scattering mechanism, we have calculated the temperature dependence of Seebeck coefficients from the measured density of carriers for $n_{32\text{ nm}}$ and $n_{11\text{ nm}}$ by using equations (1-4). Importantly, the calculated temperature dependence on Seebeck shows (Fig. 3c) that the slope of S(T) decreases when the scattering parameter varies from 2 to 1.5 to 1. This result agrees qualitatively with the decreasing slope of the measured Seebeck coefficients for thinner films (see Fig. 1c). Different values of r represent different scattering mechanisms. For example, r=0, ½, 1, and 2 can be considered for calculation of Seebeck coefficients when acoustic phonon scattering (or alloy, point- defect scattering), neutral impurities, optical phonon scattering, and the charge impurity scattering, respectively, dominate the

conduction process[53–55]. Hence, it is likely from our analysis that the scattering mechanism is changing continuously when the thickness of the film reduces gradually. AFM topography images show that the surface of all the films is extremely flat, and there is no sign of any change of the surface morphology as a function of film thickness (see Fig. S5). The change in the scattering mechanism might be related to different kinds of defects in the film that take part in the process of conduction.

In general, the formation of EDL at the film surface is considered as one of the major factors which reduce the density of carriers by shifting the Fermi level for thinner Nb:STO films[29]. It is generally considered that negatively charged EDL is formed at the surface of electron-doped STO films, most probably because of Sr vacancies at the surface[35]. Formation of such EDL at the surface was further supported experimentally[56] with synchrotron-based *in situ* ambient pressure x-ray photoelectron spectroscopy experiments[35]. So, the larger the width of EDL the lower the density of carriers. It is important to note that the width of the EDL might vary depending on (i) the type of redox chemical reactions (oxidation/reduction) happening at the surfaces[35,56] (ii) the doping concentration as the width of EDL is proportional to $1/\sqrt{n}$ [34,57] and (iii) the dielectric constant (ε)[29]. A recent study on La-doped $SrTiO_3$ films suggests that the thickness of the dead layer is independent of the doping concentration and charge carrier density[34]. This contradicts the role of the EDL effect to the formation of a dead-layer of constant thickness, as the width of EDL should be proportion to $1/\sqrt{n}$. An investigation on the thickness dependence on the dielectric constant for ultrathin Nb:STO films might provide a better understanding of the continuous decrease of carriers and the dead-layer as the width of the EDL is related to the dielectric constant. The dielectric constant of $SrTiO_3$ film decreases with decreasing thicknesses ranging from 2.5 µm to 25 nm[58] but the trend is not known for the films between 25 to 2 nm thicknesses, where a sharp drop of conductivity is observed. Although the origin of the continuous decrease of the carriers with decreasing film thickness and the formation of the dead-layer remains unclear, our experimental results suggest that the scattering mechanism are important factors when the thickness of the films reduces to a few unit cells.

3. Conclusions

A set of Nb:STO films with variable thicknesses ranging from 68 to 2 nm were deposited on top of LSAT single crystal substrates using PLD and their structural, electronic, and thermoelectric properties were studied. The films show a slight increase in tetragonality with decreasing film thickness. We have observed

a gradual drop in both the conductivity and Seebeck coefficients of Nb:STO films as the film thickness decreases. The drop of conductivity can be understood in terms of the decrease of the density and mobility of charge carriers, while the drop of the Seebeck coefficient can be interpreted from the continuous change of the scattering mechanism. This study opens up the scope to further study the correlation among film thickness, dielectric constant, and electron depletion layer in the case of free-standing Nb:STO membrane, which will provide a comprehensive understanding of its correlation with the electronic transport properties.

Acknowledgments

The research leading to these results has received funding from the European Union´s H2020 Programme under Grant Agreement no 824072 – HARVESTORE. AC thanks to Prof. Francisco Rivadulla from CIQUS (Centro Singular de Investigación en Química Biolóxica e Materiais Moleculares, Departamento de Química-Física, Universidade de Santiago de Compostela, Santiago de Compostela 15782, Spain) for helping with the Seebeck effect measurements.

Conflict of interest

The authors declare no conflict of interest

CrediT authorship contribution statement

Fabrication of thin films- **A.C. and S.S.**; DFT-based calculations- **Z.L. and I.E.C**; XRD, XRR, RSM, and AFM measurements- **A.C.**; Electronic and thermoelectric transport measurements- **A.C**.; Thickness measurement by ellipsometry technique, AFM, and electronic conductivity- **F.B., A.M., and A.T.**; Calculation of Seebeck coefficients from the measured charge carrier density- **A.C. and E.C-A.**; Supervision of work- **D.V.C., Y.C., and N.P.**; Data analysis and manuscript writing- **A.C.**, **D.V.C.**, and **N.P.**; All the authors contributed in the manuscript, reviewed, and edited.

References

1 K. Shibuya, T. Ohnishi, T. Sato and M. Lippmaa, *J. Appl. Phys.*, 2007, **102**, 083713.

2 J. H. Haeni, P. Irvin, W. Chang, R. Uecker, P. Reiche, Y. L. Li, S. Choudhury, W. Tian, M. E. Hawley, B. Craigo, A. K. Tagantsev, X. Q. Pan, S. K. Streiffer, L. Q. Chen, S. W. Kirchoefer, J. Levy and D. G. Schlom, *Nature*, 2004,

430, 758–761.

3 D. E. Grupp and A. M. Goldman, *Science (80-.).*, 1997, **276**, 392–394.

4 E. Meirzadeh, D. V. Christensen, E. Makagon, H. Cohen, I. Rosenhek-Goldian, E. H. Morales, A. Bhowmik, J. M. G. Lastra, A. M. Rappe, D. Ehre, M. Lahav, N. Pryds and I. Lubomirsky, *Adv. Mater.*, 2019, **31**, 1904733.

5 P. Zubko, G. Catalan, A. Buckley, P. R. L. Welche and J. F. Scott, *Phys. Rev. Lett.*, 2007, **99**, 167601.

6 H. Ohta, S. Kim, Y. Mune, T. Mizoguchi, K. Nomura, S. Ohta, T. Nomura, Y. Nakanishi, Y. Ikuhara, M. Hirano, H. Hosono and K. Koumoto, *Nat. Mater.*, 2007, **6**, 129–134.

7 D. V. Christensen, Y. Frenkel, Y. Z. Chen, Y. W. Xie, Z. Y. Chen, Y. Hikita, A. Smith, L. Klein, H. Y. Hwang, N. Pryds and B. Kalisky, *Nat. Phys.*, 2019, **15**, 269–274.

8 P. Moetakef, J. R. Williams, D. G. Ouellette, A. P. Kajdos, D. Goldhaber-Gordon, S. J. Allen and S. Stemmer, *Phys. Rev. X*, 2012, **2**, 021014.

9 J. F. Schooley, W. R. Hosler and M. L. Cohen, *Phys. Rev. Lett.*, 1964, **12**, 474–475.

10 Y. Kozuka, Y. Hikita, C. Bell and H. Y. Hwang, *Appl. Phys. Lett.*, 2010, **97**, 012107.

11 S. Kobayashi, Y. Mizumukai, T. Ohnishi, N. Shibata, Y. Ikuhara and T. Yamamoto, *ACS Nano*, 2015, **9**, 10769–10777.

12 J. Son, P. Moetakef, B. Jalan, O. Bierwagen, N. J. Wright, R. Engel-Herbert and S. Stemmer, *Nat. Mater.*, 2010, **9**, 482–484.

13 C. Baeumer, N. Raab, T. Menke, C. Schmitz, R. Rosezin, P. Müller, M. Andrä, V. Feyer, R. Bruchhaus, F. Gunkel, C. M. Schneider, R. Waser and R. Dittmann, *Nanoscale*, 2016, **8**, 13967–13975.

14 H. Ohta, T. Mizuno, S. Zheng, T. Kato, Y. Ikuhara, K. Abe, H. Kumomi, K. Nomura and H. Hosono, *Adv. Mater.*, 2012, **24**, 740–744.

15 S. Shimizu, S. Ono, T. Hatano, Y. Iwasa and Y. Tokura, *Phys. Rev. B - Condens. Matter Mater. Phys.*, 2015, **92**, 165304.

16 H. Ohta, Y. Masuoka, R. Asahi, T. Kato, Y. Ikuhara, K. Nomura and H. Hosono, *Appl. Phys. Lett.*, 2009, **95**, 113505.

17 Y. Zhang, B. Feng, H. Hayashi, T. Tohei, I. Tanaka, Y. Ikuhara and H. Ohta, *J. Appl. Phys.*, 2017, **121**, 185102.

18 Y. Zhang, B. Feng, H. Hayashi, C. P. Chang, Y. M. Sheu, I. Tanaka, Y. Ikuhara and H. Ohta, *Nat. Commun.*, 2018, **9**, 2224.

19 S. Bhansali, W. Khunsin, A. Chatterjee, J. Santiso, B. Abad, M. Martin-Gonzalez, G. Jakob, C. M. Sotomayor Torres and E. Chávez-Angel, *Nanoscale Adv.*, 2019, **1**, 3647–3653.

20 A. Sarantopoulos, E. Ferreiro-Vila, V. Pardo, C. Magén, M. H. Aguirre and F. Rivadulla, *Phys. Rev. Lett.*, 2015, **115**, 166801.

21 K. H. Lee, A. Ishizaki, H. Ohta and K. Koumoto, *Int. Conf. Thermoelectr. ICT, Proc.*, 2007, 136–139.

22 Q. Wang, Y. Fang, H. Yin and J. Li, *Chem. Commun.*, 2015, **51**, 1594–1596.

23 D. J. Keeble, S. Wicklein, L. Jin, C. L. Jia, W. Egger and R. Dittmann, *Phys. Rev. B - Condens. Matter Mater. Phys.*, 2013, **87**, 195409.

24 E. Breckenfeld, A. B. Shah and L. W. Martin, *J. Mater. Chem. C*, 2013, **1**, 8052–8059.

25 D. J. Keeble, S. Wicklein, R. Dittmann, L. Ravelli, R. A. MacKie and W. Egger, *Phys. Rev. Lett.*, 2010, **105**, 226102.

26 T. Ohnishi, M. Lippmaa, T. Yamamoto, S. Meguro and H. Koinuma, *Appl. Phys. Lett.*, 2005, **87**, 241919.

27 S. Wicklein, A. Sambri, S. Amoruso, X. Wang, R. Bruzzese, A. Koehl and R. Dittmann, *Appl. Phys. Lett.*, 2012, **101**, 131601.

28 E. Breckenfeld, R. Wilson, J. Karthik, A. R. Damodaran, D. G. Cahill and L. W. Martin, *Chem. Mater.*, 2012, **24**, 331–337.

29 A. Ohtomo and H. Y. Hwang, *Appl. Phys. Lett.*, 2004, **84**, 1716–1718.

30 J. Ravichandran, W. Siemons, D. W. Oh, J. T. Kardel, A. Chari, H. Heijmerikx, M. L. Scullin, A. Majumdar, R. Ramesh and D. G. Cahill, *Phys. Rev. B - Condens. Matter Mater. Phys.*, 2010, **82**, 165126.

31 L. Iglesias, A. Sarantopoulos, C. Magén and F. Rivadulla, *Phys. Rev. B*, 2017, **95**, 165138.

32 T. A. Cain, A. P. Kajdos and S. Stemmer, *Appl. Phys. Lett.*, 2013, **102**, 182101.

33 M. Apreutesei, R. Debord, M. Bouras, P. Regreny, C. Botella, A. Benamrouche, A. Carretero-Genevrier, J. Gazquez, G. Grenet, S. Pailhès, G. Saint-Girons and R. Bachelet, *Sci. Technol. Adv. Mater.*, 2017, **18**, 430–435.

34 Y. J. Shin, C. Lau, S. Lee, F. J. Walker and C. H. Ahn, *Appl. Phys. Lett.*, 2019, **115**, 161601.

35 M. Andrä, H. Bluhm, R. Dittmann, C. M. Schneider, R. Waser, D. N. Mueller and F. Gunkel, *Phys. Rev. Mater.*, 2019, **3**, 044604.

36 J. S. Jeong, P. Ambwani, B. Jalan, C. Leighton and K. A. Mkhoyan, *ACS Nano*, 2013, **7**, 4487–4494.

37 D. D. Cuong, B. Lee, K. M. Choi, H. S. Ahn, S. Han and J. Lee, *Phys. Rev. Lett.*, 2007, **98**, 115503.

38 K. Eom, E. Choi, M. Choi, S. Han, H. Zhou and J. Lee, *J. Phys. Chem. Lett.*, 2017, **8**, 3500–3505.

39 E. Langenberg, E. Ferreiro-Vila, V. Leborán, A. O. Fumega, V. Pardo and F. Rivadulla, *APL Mater.*, 2016, **4**, 104815.

40 J. Sun, A. Ruzsinszky and J. Perdew, *Phys. Rev. Lett.*, 2015, **115**, 036402.

41 G. Kresse and J. Hafner, *Phys. Rev. B*, 1993, **47**, 558–561.

42 S. R. S. Kumar, A. Z. Barasheed and H. N. Alshareef, *ACS Appl. Mater. Interfaces*, 2013, **5**, 7268–7273.

43 Y. Chen, N. Pryds, J. E. Kleibeuker, G. Koster, J. Sun, E. Stamate, B. Shen, G. Rijnders and S. Linderoth, *Nano Lett.*, 2011, **11**, 3774–3778.

44 M. Jonson and G. D. Mahan, *Phys. Rev. B*, 1980, **21**, 4223–4229.

45 T. Sakudo and H. Unoki, *Phys. Rev. Lett.*, 1971, **26**, 851–853.

46 F. Trier, D. V. Christensen and N. Pryds, *J. Phys. D. Appl. Phys.*, 2018, **51**, 293002.

47 B. Zhang, J. Wang, T. Zou, S. Zhang, X. Yaer, N. Ding, C. Liu, L. Miao, Y. Li and Y. Wu, *J. Mater. Chem. C*, 2015, **3**, 11406–11411.

48 H. Ledbetter, M. Lei and S. Kim, *Phase Transitions*, 1990, **23**, 61–70.

49 G. J. Snyder and E. S. Toberer, *Nat. Mater.*, 2008, **7**, 105–114.

50 J. Sun and D. J. Singh, *APL Mater.*, 2016, **4**, 104803.

51 T. Okuda, K. Nakanishi, S. Miyasaka and Y. Tokura, *Phys. Rev. B - Condens. Matter Mater. Phys.*, 2001, **63**, 113104.

52 K. Durczewski and M. Ausloos, *Phys. Rev. B - Condens. Matter Mater. Phys.*, 2000, **61**, 5303–5310.

53 P. Komar, E. Chávez-Ángel, C. Euler, B. Balke, U. Kolb, M. M. Müller, H. J. Kleebe, G. H. Fecher and G. Jakob, *APL Mater.*, 2016, **4**, 104902.

54 H. Xie, H. Wang, Y. Pei, C. Fu, X. Liu, G. J. Snyder, X. Zhao and T. Zhu, *Adv. Funct. Mater.*, 2013, **23**, 5123–5130.

55 F. G. Aliev, V. V. Kozyrkov, V. V. Moshchalkov, R. V. Scolozdra and K. Durczewski, *Z. Phys. B - Condens. Matter*, 1990, **80**, 353–357.

56 M. Andrä, F. Dvořák, M. Vorokhta, S. Nemšák, V. Matolín, C. M. Schneider, R. Dittmann, F. Gunkel, D. N.

Mueller and R. Waser, *APL Mater.*, 2017, **5**, 056106.

57 R. F. Pierret, *Semiconductor Device Fundamentals*, Addison-Wesley, 1996.

58 H. C. Li, W. Si, A. D. West and X. X. Xi, *Appl. Phys. Lett.*, 1998, **73**, 464–466.

Supporting Information (SI)

I: Calculation of out-of-plane lattice constants by using Poisson ratio

Calculation of the expected *c*-parameter of film from Poisson ratio (ν) is obtained by using the following relations:

$$\nu = -\frac{\epsilon_t}{\epsilon_l}$$

$$\epsilon_t = \frac{(out-of-plane,\ c)_{film} - c_{bulk}}{c_{bulk}}$$

$$\epsilon_l = \frac{(in-plane, a)_{film} - a_{bulk}}{a_{bulk}}$$

Assuming a material is stretched or contracted in axial direction against in-plane compressive or tensile strain, then ν is given by the ratio of transverse strain (ϵ_t) to axial strain (ϵ_l)[1]. In our case, films are epitaxial and compressively strained (-1.33%) on LSAT substrates. Hence, the in-plane (a_{film}) parameters of the films are same as LSAT substrates (LSAT, a = 3.870 Å) and the a-parameter of bulk $SrTi_{0.94}Nb_{0.06}O_3$ is known, $a_{bulk} = 3.922$ Å (see main text[2]). Hence, ϵ_l can be calculated. On the other hand, $\nu = 0.23$ is known for standard perovskites (see main text[3]) and c_{bulk} is known for $SrTi_{0.94}Nb_{0.06}O_3$. Therefore, theoretical c_{film} value can be calculated considering an elastic strain.

II: Additional tables

Table S1 Calculated parameters obtained from DFT-based calculations by using a fixed in-plane (3.870 Å) and variable out-of-plane (3.870, 3.906, 3.970 and 3.980 Å) lattice constants of Nb:STO bulk structure.

c-parameter (Å)	η-chemical potential (eV)	*n* ($\times 10^{21}$, cm^{-3})	Effective mas $m_e(m_0)$ G-Z	Effective mas $m_h(m_0)$ G-M	Ti-d orbital position
3.870	-1.146	2.057	0.709 (G-M)	-2.626	$d_{xy}=d_{xz}=d_{yz}$ (at gamma point), Δd=0 eV
3.906	-1.140	2.104	0.318	-0.756	$d_{xy}>d_{xz}=d_{yz}$ (at gamma point), Δd=0.0122 eV
3.970	-1.121	2.019	0.337	-0.784	$d_{xy}>d_{xz}=d_{yz}$ (at gamma point), Δd=0.0377 eV
3.980	-1.117	2.056	0.339	-0.782	$d_{xy}>d_{xz}=d_{yz}$ (at gamma point), Δd=0.0432 eV

Table S2 *calculated chemical potential (η) and Seebeck coefficients (S) at 290K from the measured density of charge carriers (n) by using equation (1-4) in the main text for 31 and 11 nm thick Nb:STO films at variable electron band degeneracy (z) and scattering parameter (r). calculations are done by assuming a fixed effective mass of electrons m* (=1.1m_0, where m_0 is the rest mass of electrons).*

Thickness (nm)	*n* (cm^{-3})	|η| (ev)		*S* (µV/K) for *z*=6			*S* (µV/K) for *z*=4		
		z=6	*z*=4	*r*=1	*r*=1.5	*r*=2	*r*=1	*r*=1.5	*r*=2
32	1.7×10^{21}	0.28	0.30	-59	-73	-87	-46	-57	-68
11	9.5×10^{20}	0.15	0.20	-86	-105	-124	-67	-83	-98

Table S3 Lattice parameters, and calculated band gap of 6%Nb-doped $SrTiO_3$ at the SCAN meta-GGA level.

Lattice parameter (Å)	3.87	3.906	3.97	3.98
Band gap (eV)	1.806	1.797	1.735	1.728

III: Additional figures

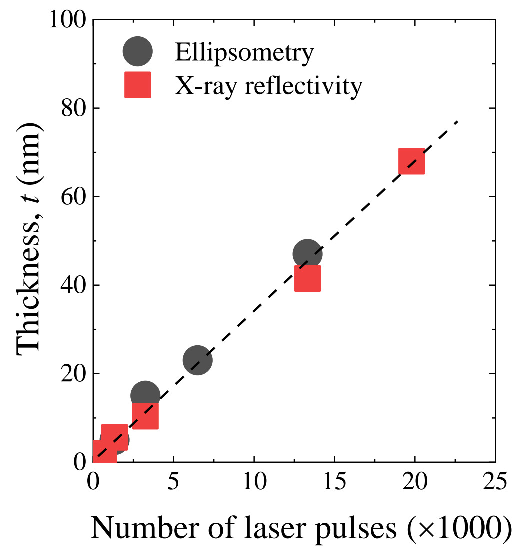

Fig. S1. *Thickness measurements of the Nb:STO films on LSAT substrates by using x-ray reflectivity and ellipsometry techniques.*

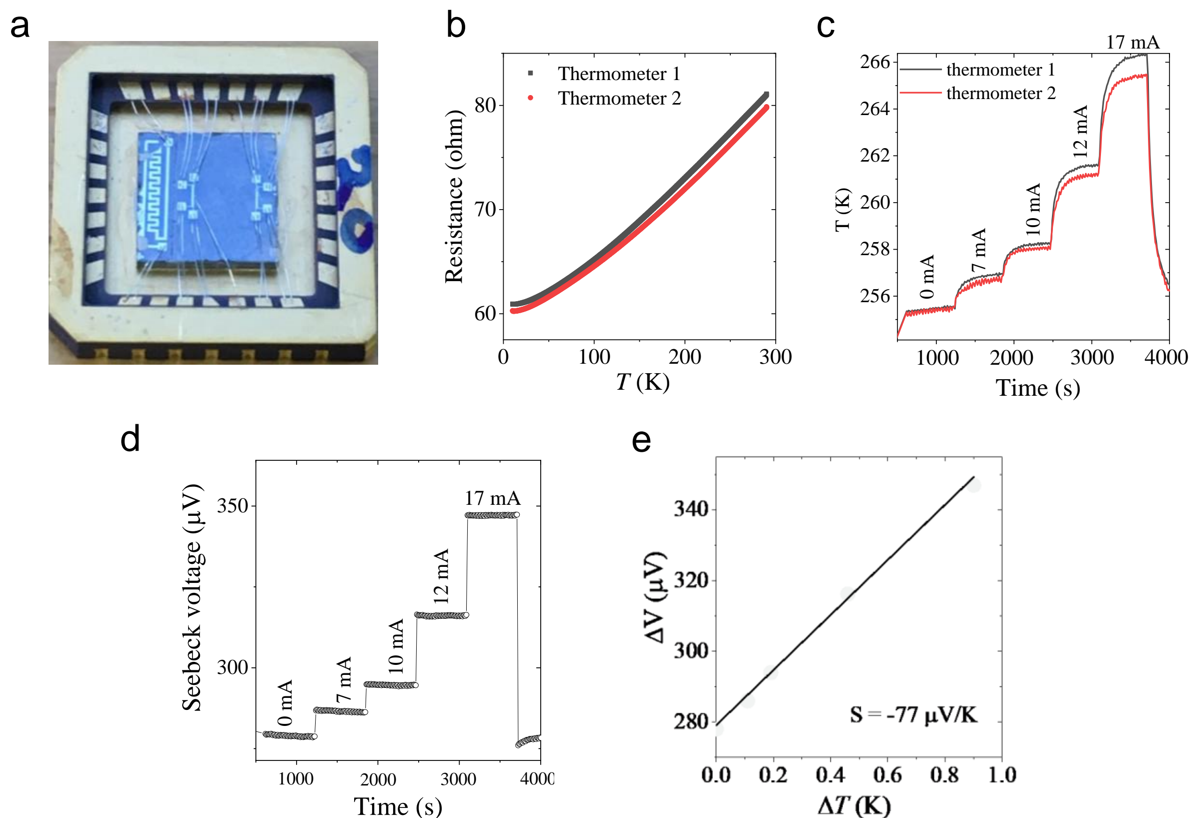

Fig. S2. *Schematic illustration of the Seebeck effect measurement on Nb:STO thin films. A Pt heater and two Pt-resistors/thermometers were patterned on top of the film surface by using optical lithography techniques. a - An actual image of the wire-boned Nb:STO film prepared on a chip-carrier for Seebeck coefficient measurement. b- Resistance calibration of the two Pt-resistors as a function of temperature. These files were later used to define temperature difference. c- Real time temperature measurement of the two-resistors when a variable current applied to the Pt heater and, d- at the same time Seebeck voltage measurements. e- Seebeck coefficients were calculated from the slope of the ΔV vs ΔT curve.*

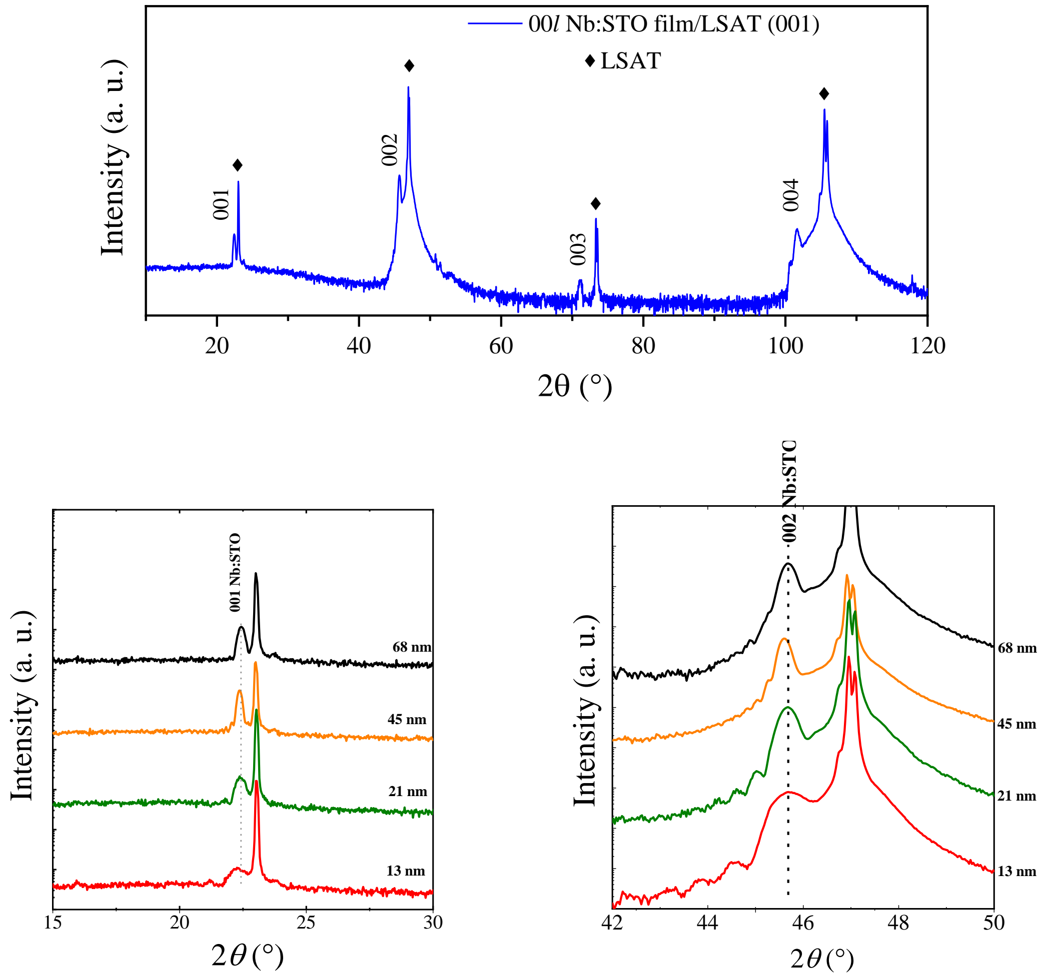

Fig. S3. *X-ray diffraction patterns of Nb:STO films deposited on LSAT-001 substrates.*

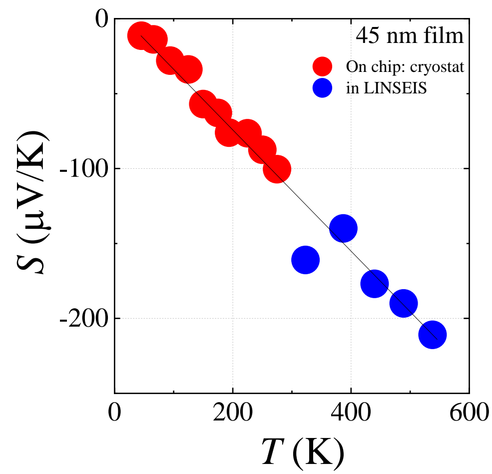

Fig. S4. *Seebeck coefficient measurements of Nb:STO films by two different techniques over a long range of temperature: on-chip Seebeck measurement in a cryostat between 20-300 K and in a LINSEIS instrument within 300-550 K.*

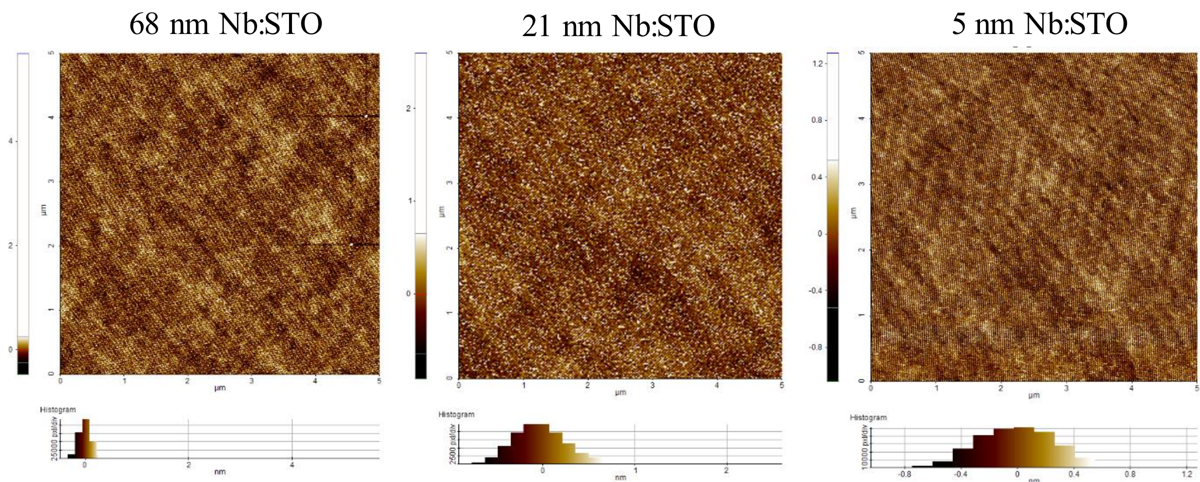

Fig. S5. AFM-topography images of Nb-doped $SrTiO_3$ films on LSAT substrates.

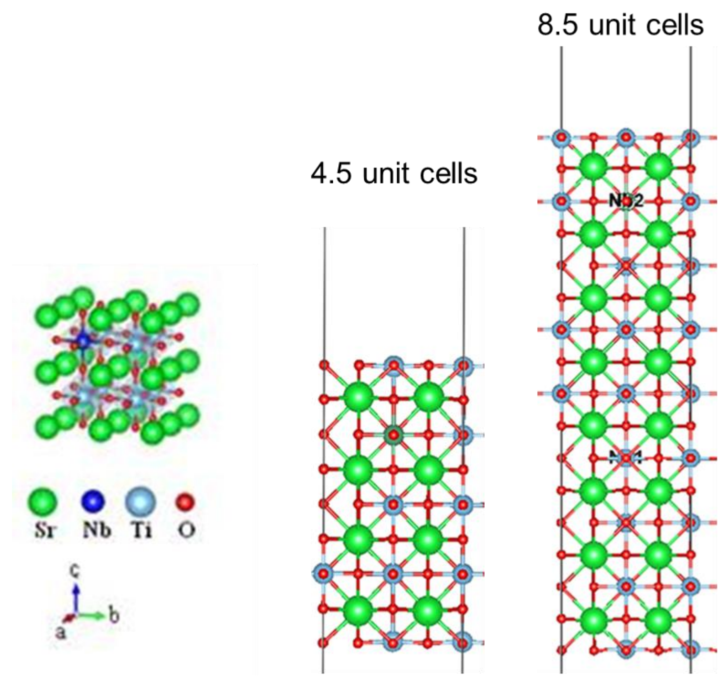

Fig. S6. Bulk crystal structures of Nb-doped $SrTiO_3$, and unit cells of Nb-doped $SrTiO_3$ films were considered for electronic band structure calculations.

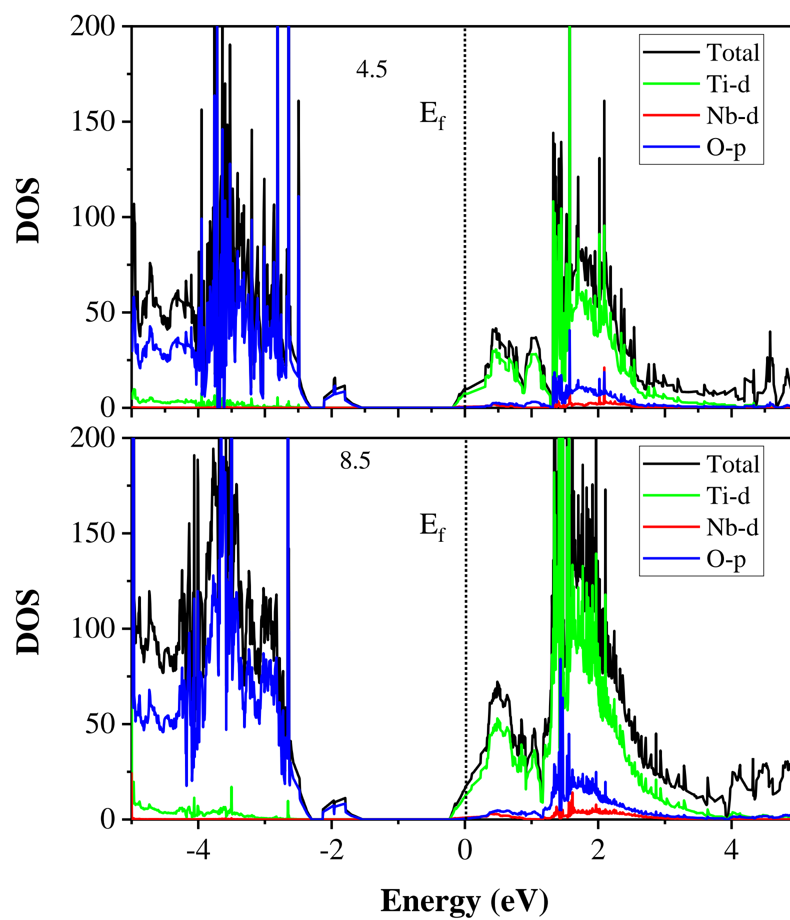

Fig. S7. Calculated electronic band structures for 4.5, and 8.5 unit cells thick Nb-doped $SrTiO_3$ films.

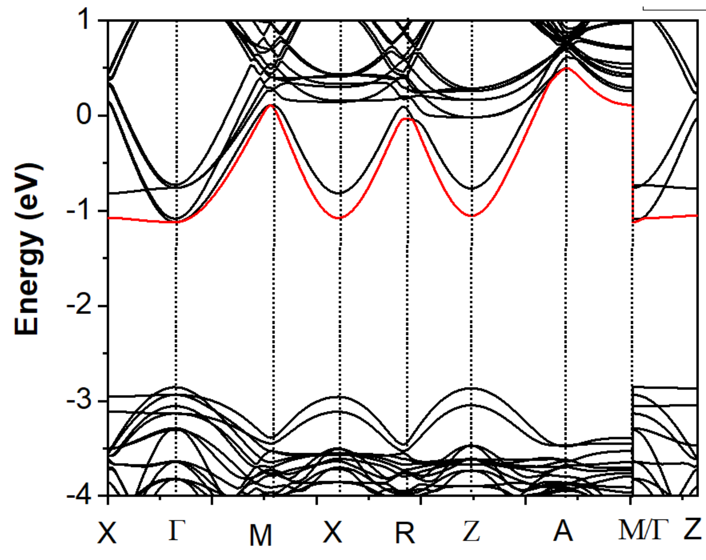

Fig. S8 The effective mass calculation by fitting a quadratic function ($y=A+Bx+Cx^2$) at the band edge from the first conduction band as highlighted by the red-line.